catalysts

MDPI

Article

Influence of Cs Promoter on Ethanol Steam-Reforming Selectivity of Pt/m-ZrO_2 Catalysts at Low Temperature

Zahra Rajabi [1], Li Jones [1], Michela Martinelli [2], Dali Qian [3], Donald C. Cronauer [4], A. Jeremy Kropf [4], Caleb D. Watson [1] and Gary Jacobs [1,5,*]

[1] Department of Biomedical Engineering and Chemical Engineering, University of Texas at San Antonio, One UTSA Circle, San Antonio, TX 78249, USA; zahra.rajabi@utsa.edu (Z.R.); bae233@my.utsa.edu (L.J.); caleb.watson378@gmail.com (C.D.W.)
[2] University of Kentucky Center for Applied Energy Research, 2540 Research Park Drive, Lexington, KY 40511, USA; michela.martinelli@uky.edu
[3] University of Kentucky Electron Microscopy Center, University of Kentucky, ASTeCC Building—Room A004, Lexington, KY 40508, USA; dali.qian@uky.edu
[4] Argonne National Laboratory, Lemont, IL 60439, USA; dccronauer@anl.gov (D.C.C.); kropf@anl.gov (A.J.K.)
[5] Department of Mechanical Engineering, University of Texas at San Antonio, One UTSA Circle, San Antonio, TX 78249, USA
* Correspondence: gary.jacobs@utsa.edu; Tel.: +1-210-458-7080

Abstract: The decarboxylation pathway in ethanol steam reforming ultimately favors higher selectivity to hydrogen over the decarbonylation mechanism. The addition of an optimized amount of Cs to Pt/m-ZrO_2 catalysts increases the basicity and promotes the decarboxylation route, converting ethanol to mainly H_2, CO_2, and CH_4 at low temperature with virtually no decarbonylation being detected. This offers the potential to feed the product stream into a conventional methane steam reformer for the production of hydrogen with higher selectivity. DRIFTS and the temperature-programmed reaction of ethanol steam reforming, as well as fixed bed catalyst testing, revealed that the addition of just 2.9% Cs was able to stave off decarbonylation almost completely by attenuating the metallic function. This occurs with a decrease in ethanol conversion of just 16% relative to the undoped catalyst. In comparison with our previous work with Na, this amount is—on an equivalent atomic basis—just 28% of the amount of Na that is required to achieve the same effect. Thus, Cs is a much more efficient promoter than Na in facilitating decarboxylation.

Keywords: ethanol steam reforming (ESR); DRIFTS; Cs doping; zirconia; decarboxylation; decarbonylation

Citation: Rajabi, Z.; Jones, L.; Martinelli, M.; Qian, D.; Cronauer, D.C.; Kropf, A.J.; Watson, C.D.; Jacobs, G. Influence of Cs Promoter on Ethanol Steam-Reforming Selectivity of Pt/m-ZrO_2 Catalysts at Low Temperature. *Catalysts* **2021**, *11*, 1104. https://doi.org/10.3390/catal11091104

Academic Editors: Sebastiano Campisi, Sofia Capelli and Stefano Cattaneo

Received: 26 July 2021
Accepted: 10 September 2021
Published: 14 September 2021

1. Introduction

Ethanol has been used as a production automotive biofuel since the late 1970s, and US ethanol production reached approximately 5.8×10^{10} L in 2017 [1]. First-generation sources, which compete with food production, include primarily sugar cane, sugar beets, and corn, but in recent years, there has been a shift in research focus toward next-generation sources that do not compete with food production, such as cellulosic ethanol from grasses, wood, and algae [2]. For example, the production of cellulosic ethanol increased from 2014 to 2015 from 728,509 gallons to 2,181,096 gallons [3]. In the future, paper municipal waste may join the list of cellulosic sources, although currently, renewable natural gas (e.g., landfill gas) accounts for the vast majority of cellulosic fuel [4].

Light alcohols are also being considered as a chemical carrier for hydrogen for use in polymer electrolyte membrane (PEM) fuel cells, and bioethanol is particularly attractive due to its renewable production as described previously. Hydrogen production is also finding importance in the biomedical field for applications such as cancer research [5], neuromedicine [6,7], and the amelioration of oxidative stress [8,9]. One challenge in catalytically reforming ethanol that is not encountered with methanol is the C–C scission

step. A potential method to reform ethanol is to convert it to H_2, CO_2, and methane at low temperature and then to further reform methane using current commercial technology (e.g., steam reforming, autothermal reforming, etc. [10]). As shown below, decarboxylation routes in the mechanism of ethanol steam reforming improve the H_2 selectivity by as much as 50% as compared to decarbonylation routes:

$$C_2H_5OH + 3H_2O \rightarrow 2CO_2 + 6H_2 \ (\Delta H_{298}^{\circ} = 173 \text{ kJ/mol}) \quad (1)$$

$$C_2H_5OH + H_2O \rightarrow 2CO + 4H_2 \ (\Delta H_{298}^{\circ} = 55 \text{ kJ/mol}). \quad (2)$$

Significant research has been recently performed using metal nanoparticles supported on partially reducible oxides (PRO) such as CeO_2, ZrO_2, and CeO_2-ZrO_2 mixed oxides. These active oxides have high oxygen mobility, making them able to shuttle O-bound intermediates on the surface defect sites (e.g., O vacancies). The reduced defects also provide sites for the dissociation of ROH molecules such as H_2O, CH_3OH [11], and CH_3CH_2OH [12]. The synergy between metal nanoparticles and reduced defects on the active metal oxide was proposed to be responsible for the higher activity of Pt/ceria relative to Pt/alumina for ESR [13] at low temperature (300–450 °C). He et al. [14] observed that catalytic activity decreased in the following order: $Pt/CeO_2 > Pt/ZrO_2 > Pt/TiO_2 = Pt/C$. They suggested that the higher catalytic activity for Pt/CeO_2 is associated with interactions between Pt and defect sites on the support.

In the mid-2000s, Honda Research, USA, Inc. reported a significant improvement in the water–gas shift (WGS) reaction by doping Pt/ZrO_2 with Na [15]. Subsequent characterization work in conjunction with the University of Kentucky Center for Applied Energy Research showed that Na facilitates dehydrogenation of the formate intermediate through C–H bond weakening [16]. Recently, we have investigated the influence of alkali loading for the water–gas shift reaction [17]. We found that acceleration of the WGS rate occurs as a step change improvement within a certain loading range (e.g., 1.8% to 2.5% Na for 2% Pt/zirconia), which corresponded to (1) a pronounced shift in the formate ν(CH) band to lower wavenumbers in in situ infrared studies and (2) low coverage of Pt by Na, as measured by the intensity of the ν(CO) band for CO adsorbed on Pt. This electronic modification of the formate intermediate by Na was responsible for improving the decarboxylation selectivity of the formate intermediate.

Ethanol steam reforming has an important analogy with water–gas shift in that one of the adsorbed intermediates in ESR for catalysts based on PRO-supported metals is acetate, which is an analog of formate in the associative mechanism of WGS [18]. Both are polyatomic anions consisting of conjugate bases of carboxylic acids. Since enhanced decarboxylation was implied in the prior work on the effect of Na dopant level of Pt/zirconia catalysts, a study was undertaken to examine the effect of Na for low-temperature ethanol steam reforming. The work showed that decarboxylation of the acetate intermediate was favored by the addition of Na and that this modification occurred in precisely the same Na loading range (1.8% to 2.5% Na) [19].

It was also of interest to examine Cs as a potential promoter. In a recent WGS investigation examining the loading effect [20], the addition of Cs led to greater shifts in the formate ν(CH) stretching band to lower wavenumbers than observed previously with Na. As such, at loadings of 3.9–7.2% Cs, in situ infrared studies revealed that formate decomposed in the forward direction (i.e., to H_2 and CO_2) more rapidly in steam than previously observed with Na. However, this effect did not translate to higher WGS activity, as the higher basicity of Cs resulted in a stronger affinity for CO_2, an acidic molecule, inhibiting its desorption at low temperature.

The finding that Cs promotion provides an improvement in formate decarboxylation selectivity suggests that it may provide an improvement in decarboxylation selectivity for the acetate intermediate during ethanol steam reforming at low temperature. To investigate this, in situ diffuse reflectance infrared Fourier transform spectroscopy (DRIFTS), X-ray absorption near edge spectroscopy (XANES), temperature-programmed desorption (TPD)

of adsorbed ethanol/water mixture, and fixed bed catalytic reaction testing were performed on catalysts having no Cs and loadings of Cs containing low, moderate, or high amounts. These results were further correlated with results from electron microscopy with elemental mapping, X-ray diffraction (XRD), and characterization and reaction testing data from our earlier WGS study to provide conclusions on the selectivity effect of Cs. A major aim of the paper is to determine if the optimal loading, at which promotion of the ESR selectivity occurs, matches the loading at which electronic modification of C–H bond scission of formate occurs in water–gas shift. In the case of WGS, this occurred when (a) the loading of Cs was high enough to cause the electronic modification but not so high that it covers the Pt metal function, which is responsible for H-transfer pathways. The second aim is to determine if this electronic modification occurs at a lower atomic loading than lighter promoters such as Na. By comparing catalysts with atomically equivalent loadings, the question we wish to address is whether the higher basicity of the softer Cs^+ cation results in a greater promoting effect than less basic harder cations such as Na^+. This would shed light on the ranking of alkali promoters for hydrogen production reactions such as WGS and ESR.

2. Results and Discussion

Table 1 summarizes the BET surface areas of the support/catalysts and the Pt nanoparticle sizes based on EXAFS fitting analysis. The expected surface area is based on the specific area anticipated after loading the Cs and Pt and calcining to form their corresponding oxides, assuming that they contribute to the weight and that the only contributor to the surface area is the m-ZrO_2 support. As the alkali loading is increased, the difference between the expected specific area (Expected A_S) and the measured BET surface area (Measured A_S) increases, and this indicates a fraction of pore blocking caused by the alkali. The $N_{Pt\text{-}Pt}$ value is the average coordination number of Pt with Pt in the first coordination shell. Using a correlation, the average diameter of Pt can be calculated. With increasing Cs content, the average diameter increases from 0.78 nm for the unpromoted catalyst to ≈1.3–1.4 nm at loadings of 10.4% Cs and 14.5% Cs.

Table 1. Summary of BET surface area and Pt particle size (adapted from [20] with permission from Catalysts, MDPI).

Sample Description	Expected A_S Assuming No Pore Blocking (m^2/g)	Measured A_S (BET) (m^2/g)	N Pt-Pt Metal	Est. No. of Atoms *	Est. Diam. (nm) **	Est. % Disp. (%)
m-ZrO_2	-	95.4	-	-	-	-
2% Pt/m-ZrO_2	93.2	89.6	5.2	13	0.78	92
2.9% Cs-2% Pt/m-ZrO_2	90.3	86.6	5.3	13	0.79	92
4.8% Cs-2% Pt/m-ZrO_2	88.3	78.7	6.3	22	0.93	87
5.8% Cs-2% Pt/m-ZrO_2	87.3	74.1	6.9	31	1.0	84
10.4% Cs-2% Pt/m-ZrO_2	82.7	62.1	8.2	82	1.4	73
14.5% Cs-2% Pt/m-ZrO_2	78.6	54.9	8.0	68	1.3	77

* Estimated from Jentys [21] assuming a spherical cluster morphology. ** Estimated from Marinkovic et al. [22].

Figure 1 shows the XRD profile for the support and catalysts. All the samples have the peaks associated with monoclinic zirconia. An additional peak associated with $Cs(NO_3)$ is detected at 19.8° for cesium loadings higher than 2.9%. STEM-EDX images for 2.9%Cs-2%Pt/ZrO_2 and 14.5%Cs-2%Pt/ZrO_2 are shown in Figure 2. Platinum crystallites are well dispersed for both samples, and their domain sizes range from slightly lower than 1 nm to slightly higher than 1 nm, which is in agreement with the diameters estimated by EXAFS (0.79–1.3 nm). STEM-EDX images show that Cs is well dispersed as well, with sizes comparable to that of Pt.

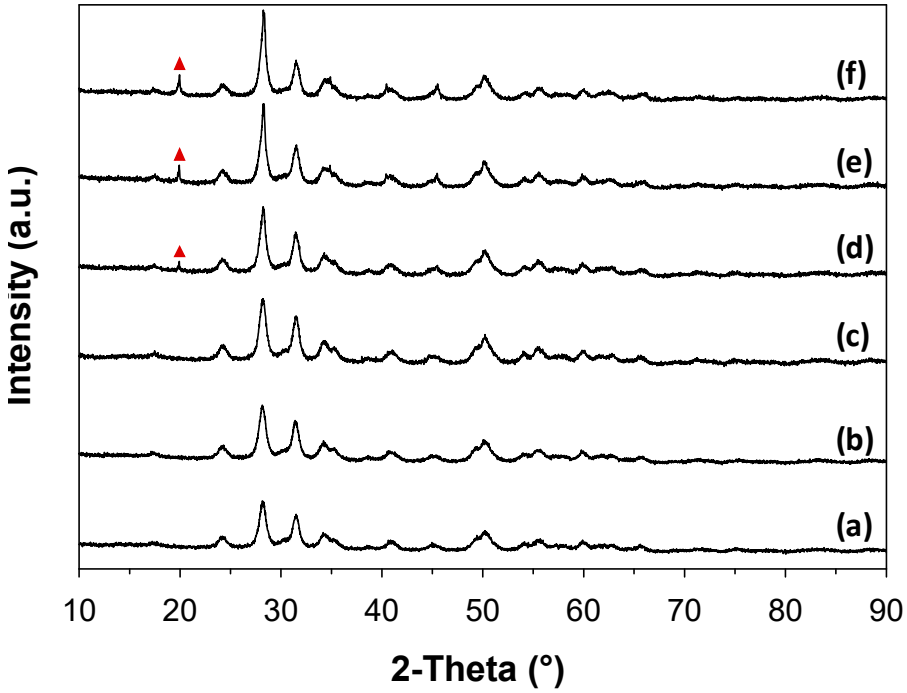

Figure 1. XRD for (**a**) ZrO_2, (**b**) 2% Pt/ZrO_2, (**c**) 0.72% Cs-2% Pt/ZrO_2, (**d**) 2.9% Cs-2% Pt/ZrO_2, (**e**) 5.8% Cs-2% Pt/ZrO_2, and (**f**) 14.5% Cs-2% Pt/ZrO_2.

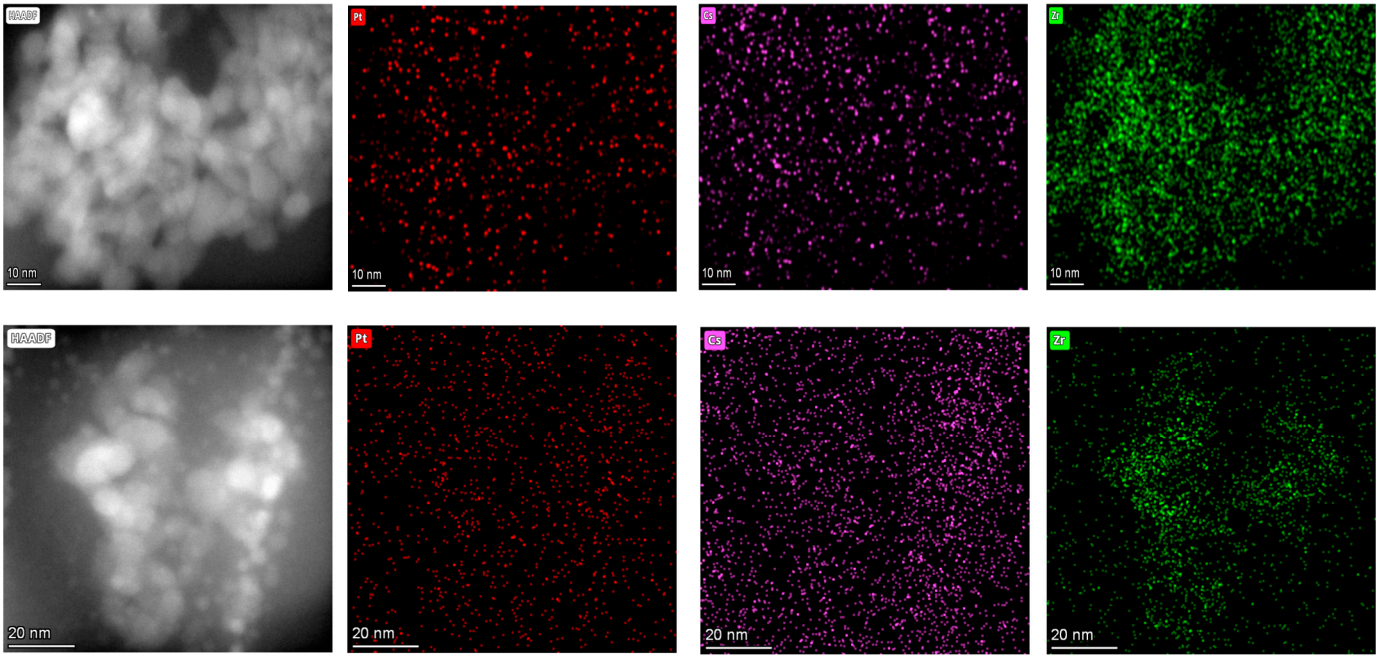

Figure 2. STEM and EDX mapping for (**top**) 2.9% Cs-2% Pt/ZrO_2 and (**bottom**) 14.5% Cs-2% Pt/ZrO_2 (mapping: red for Pt, pink for Cs and green for Zr).

TPR and TPR-MS profiles are provided in Figure 3. During activation of the catalysts in hydrogen, there is a hydrogen uptake at ≈200 °C for the reduction of Pt oxide and the spillover of hydrogen to the support to form Type II bridging OH groups. Formally, the conversion of $O_{surface}$ to $O_{surface}H$ should result in an oxidation state change on surface Zr from Zr^{4+} to Zr^{3+}, as Type II OH groups are associated with reduced defect sites on the surface shell of zirconia [23]. This process involves the decomposition of surface carbonates by decarbonylation. During this step, CO was observed to evolve from the catalyst surface.

With increasing Cs loading, the H_2 uptake peak is more pronounced, and more CO is liberated from the catalyst surface.

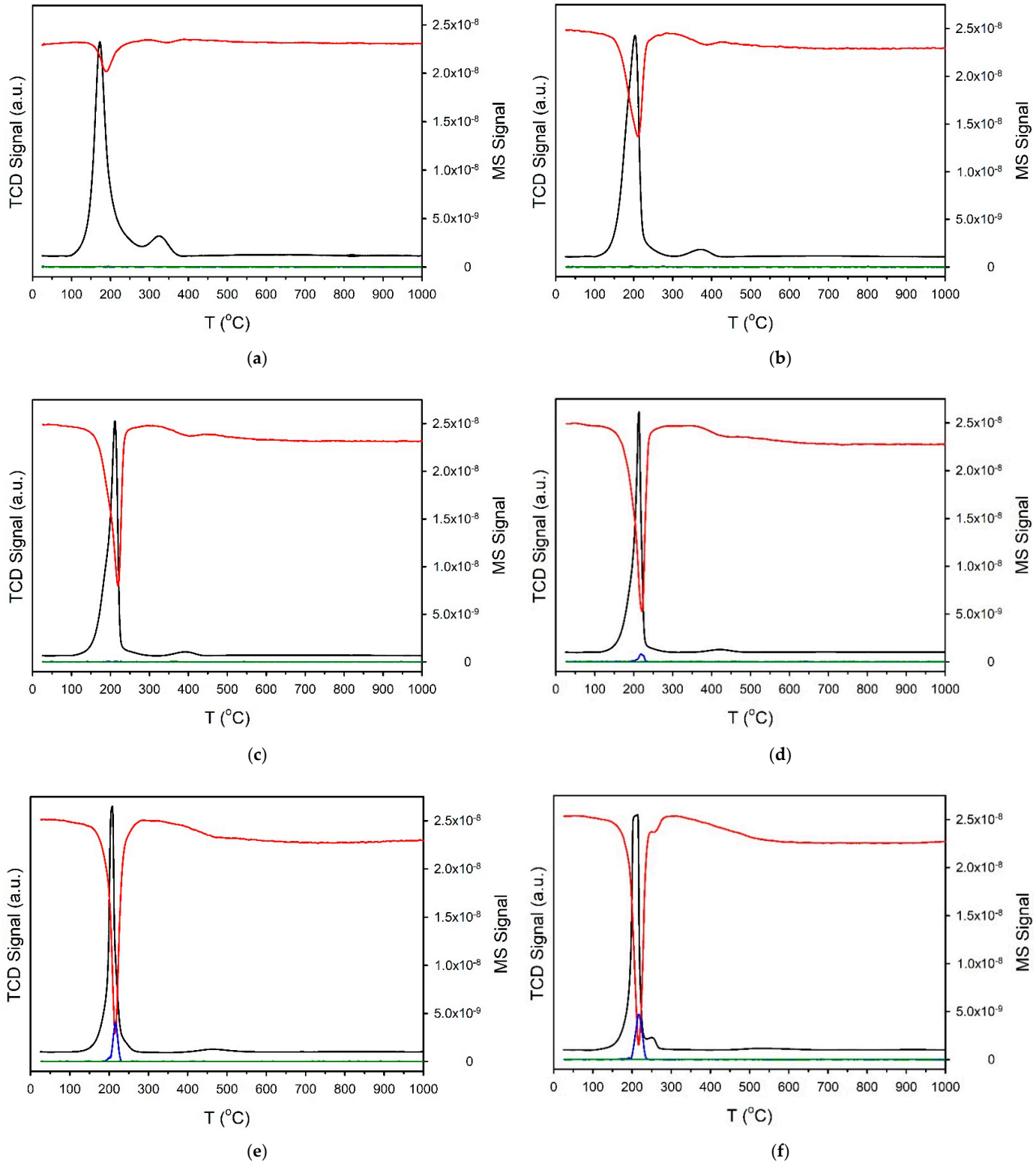

Figure 3. *Cont.*

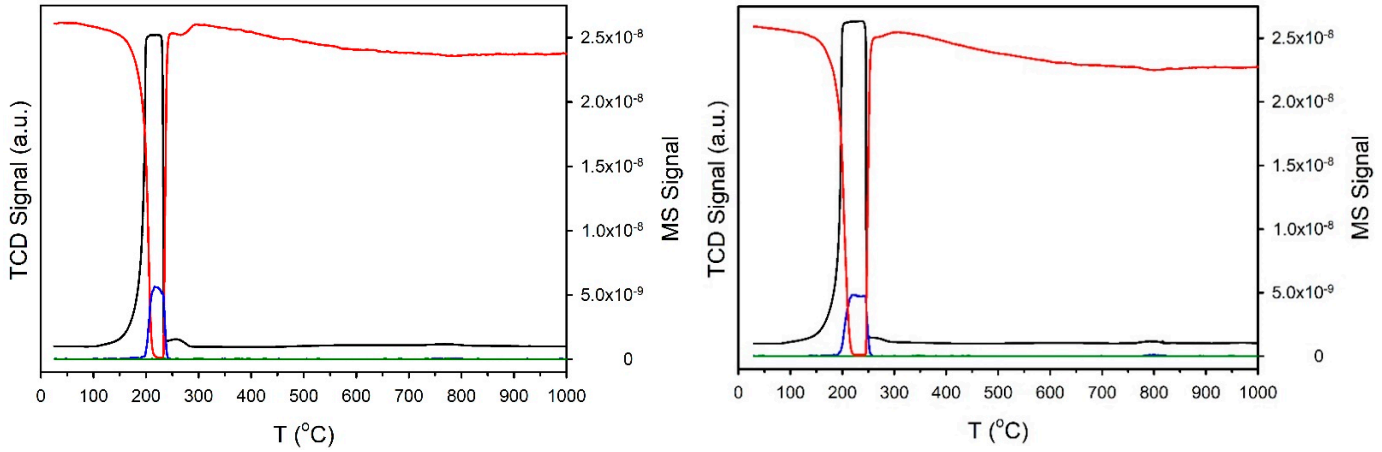

Figure 3. TCD signal (black) and MS signals of (red) H_2, (blue) CO, and (green) CO_2 during temperature-programmed reduction in 10% H_2/Ar for (**a**) 2% Pt/ZrO_2, (**b**) 2.9% Cs-2% Pt/ZrO_2, (**c**) 3.9% Cs-2% Pt/ZrO_2, (**d**) 4.8% Cs-2% Pt/ZrO_2, (**e**) 5.8% Cs-2% Pt/ZrO_2, (**f**) 7.2% Cs-2% Pt/ZrO_2, (**g**) 10.4% Cs-2% Pt/ZrO_2, and (**h**) 14.5% Cs-2% Pt/ZrO_2 (reprinted from [20]).

Figures 4–11 illustrate DRIFTS spectra for the steam reforming of ethanol at low temperature. Table 2 provides the IR band assignments from the open literature for PRO-supported noble metal particles. These assignments were used to construct Table 3, which provides the main bands observed in the spectra of the unpromoted and Cs-promoted Pt/m-ZrO_2 catalysts.

For all of the catalysts, the adsorption of ethanol produces Type II ethoxy species at the reduced defect sites on zirconia, with ν(CO) ethoxy bands forming at 1052–1057 cm^{-1}. These bands match closely with the position of Type II ν(CO) methoxy bands on ceria observed by Binet et al. [23] for adsorbed methanol following H_2 reduction at 300 °C (i.e., a procedure that results in partial reduction of ceria), while the higher wavenumber bands (1097–1111 cm^{-1}) match with the Type I ν(CO) methoxy bands observed for adsorbed methanol on unreduced ceria sites. The defect sites in m-ZrO_2 are likely confined to the vicinity of Pt nanoparticles due to the promoting effect of Pt on PRO surface shell reduction. In addition, other easily discernible bands for ethoxy species include those associated with ν(CH) and ρ(CH_3) vibrational modes, as tabulated in Table 3. The most prominent ν(CH) band occurs at ≈2970 cm^{-1}, while the rocking mode ρ(CH_3) is positioned at ≈1150 cm^{-1}.

The oxidative dehydrogenation of ethoxy species to acetate is known to occur on metal-promoted PRO. This process is analogous to the conversion of adsorbed methoxy species to formate during methanol steam reforming over the same family of catalysts [24]. Although the ν(CH) bands of ethoxy species and acetate species are similar in nature, the relative intensities change, such that the predominant ν(CH) band following the formation of acetate is positioned at ≈2930 cm^{-1}. In addition, there are asymmetric and symmetric ν(OCO) bands. The former range from primarily 1553 cm^{-1} for the unpromoted catalyst to greater than 1570 cm^{-1} for the heavily Cs doped catalysts (5.8% Cs and higher). The main band of the latter ranges from 1441 to 1398 cm^{-1}, with a generally decreasing trend in band position with Cs addition (see Table 3). The bending mode $\delta_s(CH_3)$ is also observed between ≈1300 and 1400 cm^{-1}.

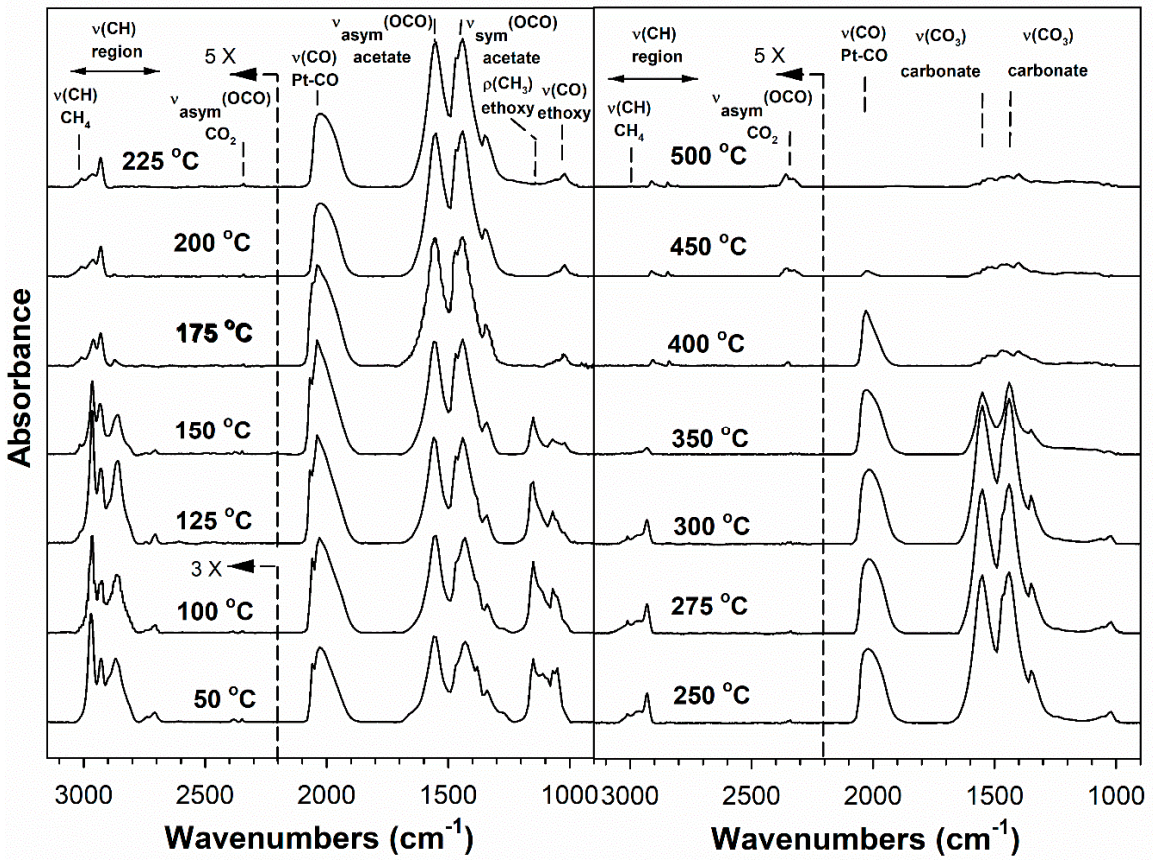

Figure 4. DRIFTS of transient ethanol steam reforming over 2% Pt/ZrO_2.

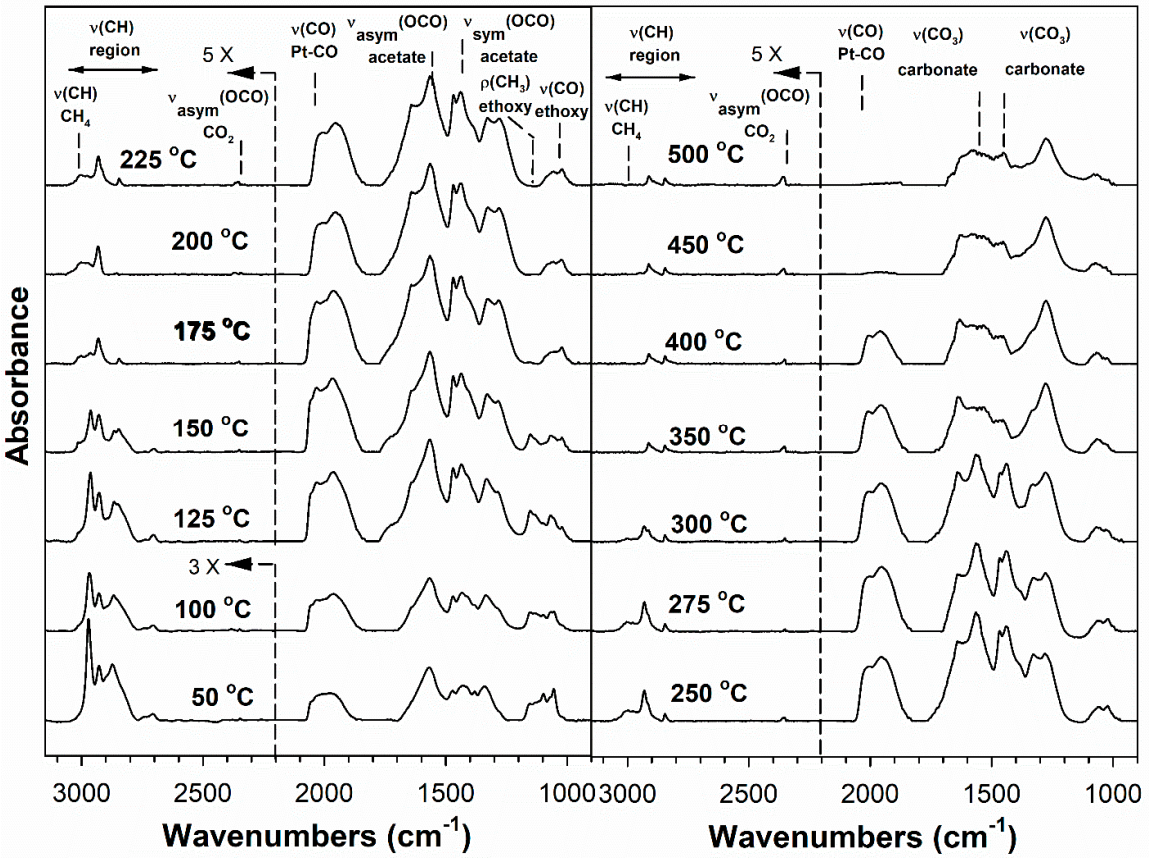

Figure 5. DRIFTS of transient ethanol steam reforming over 2.9% Cs-2% Pt/ZrO_2.

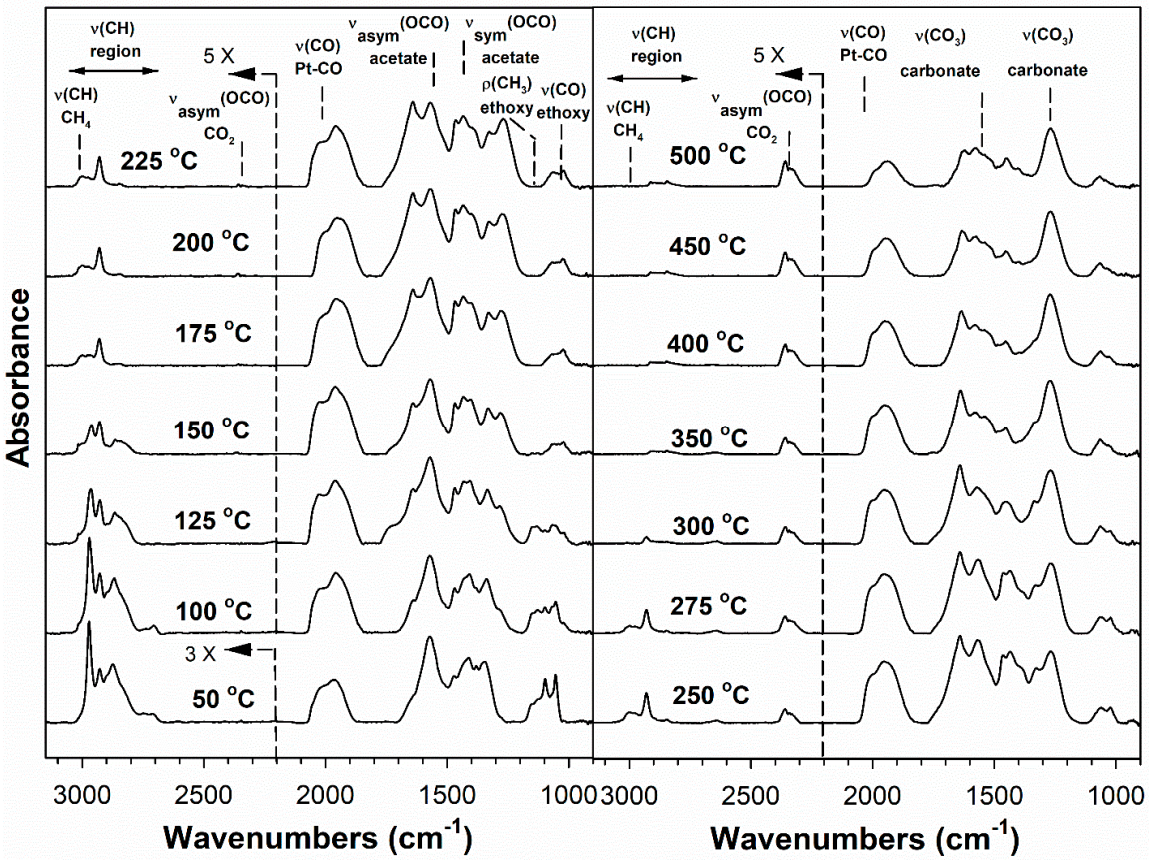

Figure 6. DRIFTS of transient ethanol steam reforming over 3.9% Cs-2% Pt/ZrO_2.

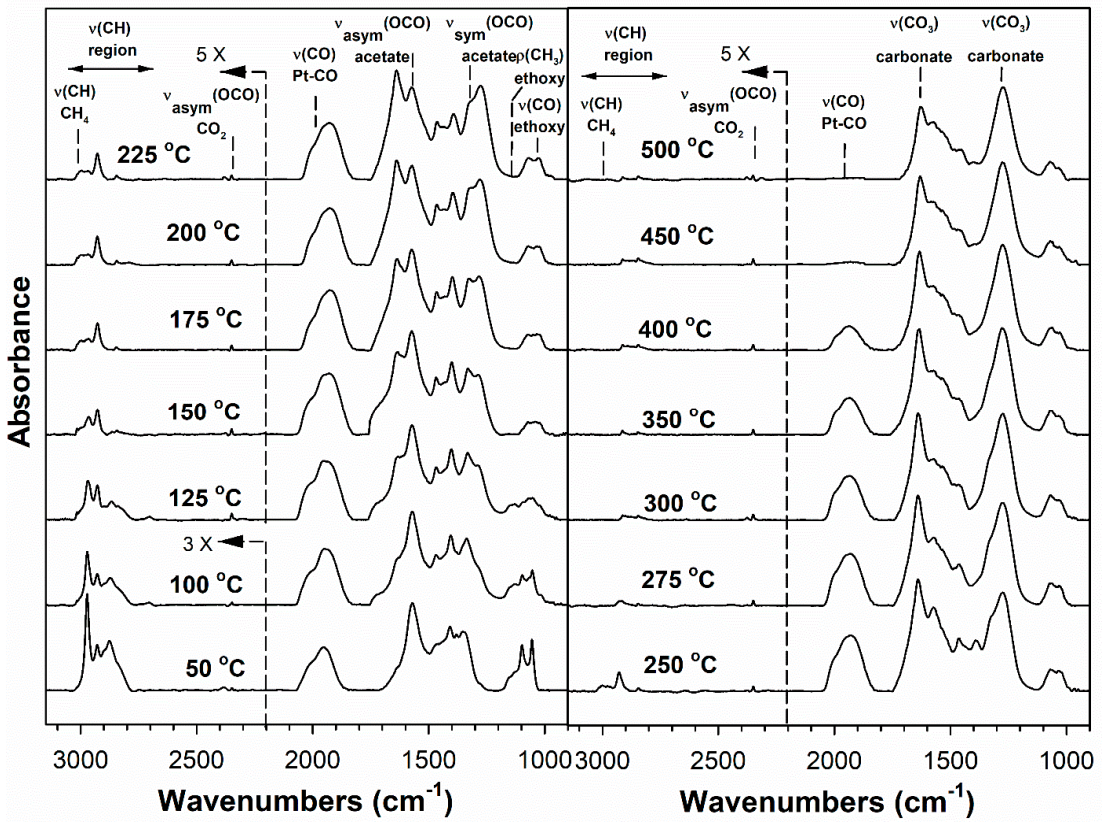

Figure 7. DRIFTS of transient ethanol steam reforming over 4.8% Cs-2% Pt/ZrO_2.

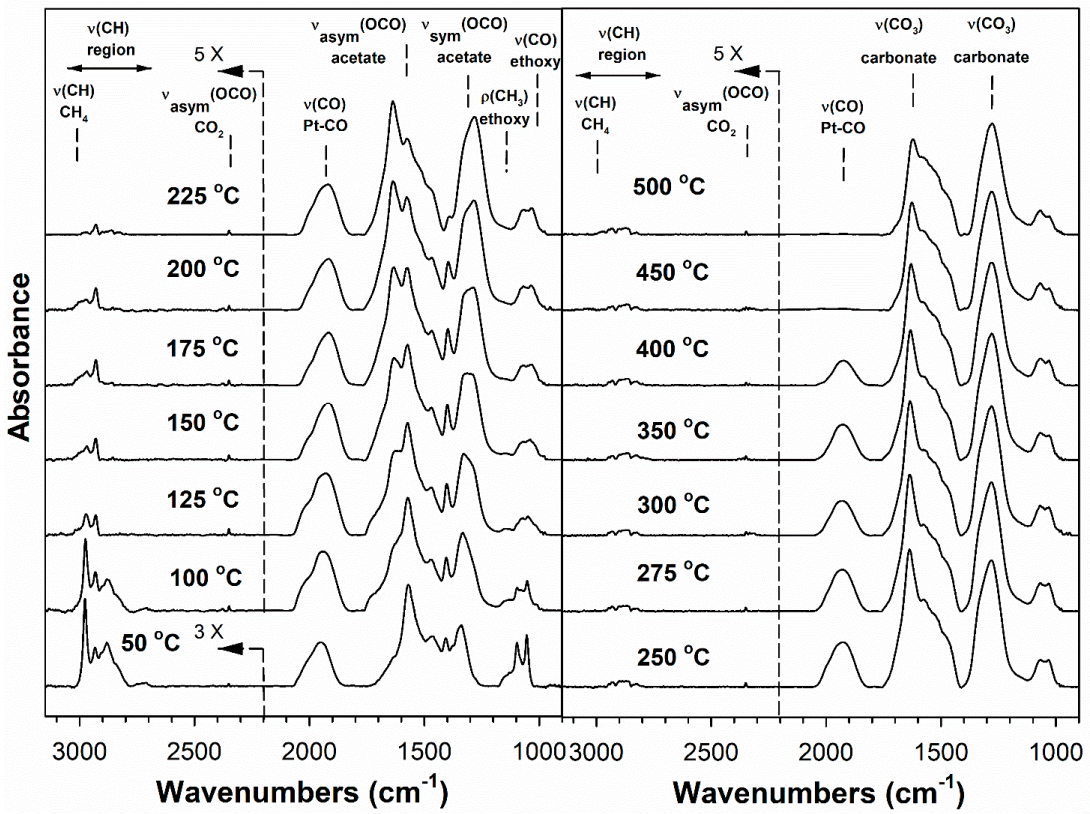

Figure 8. DRIFTS of transient ethanol steam reforming over 5.8% Cs-2% Pt/ZrO_2.

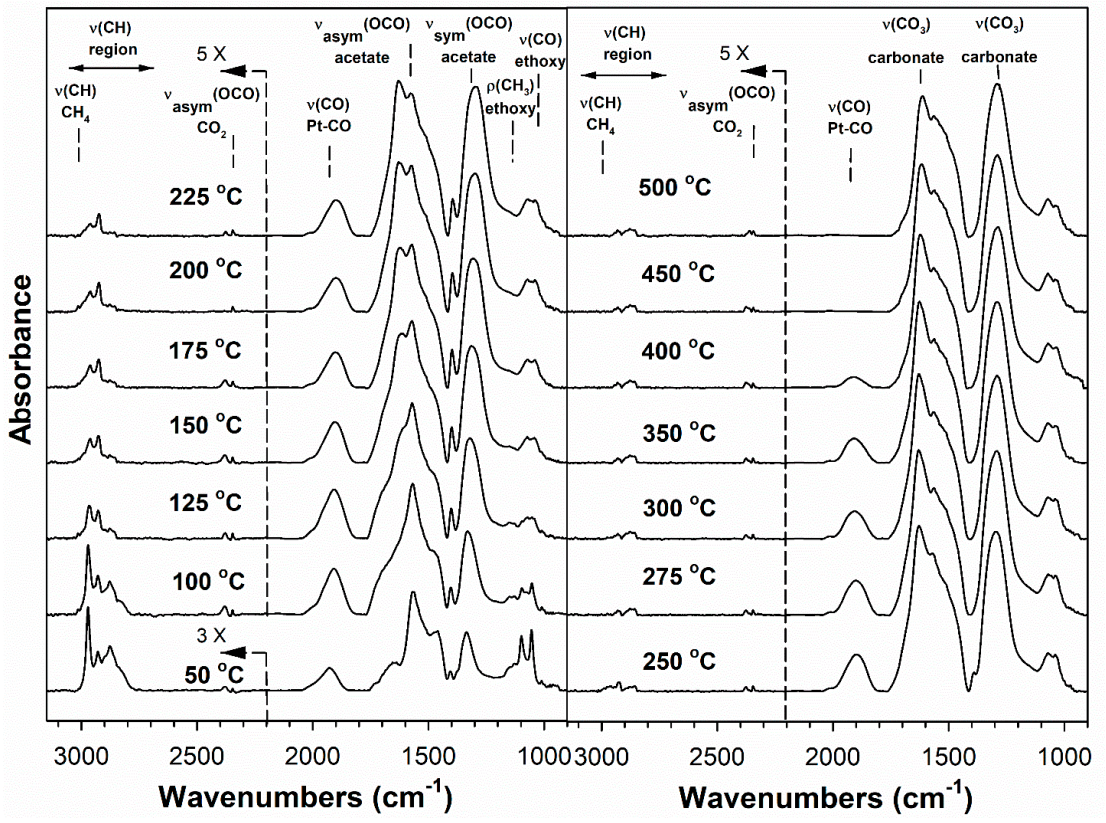

Figure 9. DRIFTS of transient ethanol steam reforming over 7.2% Cs-2% Pt/ZrO_2.

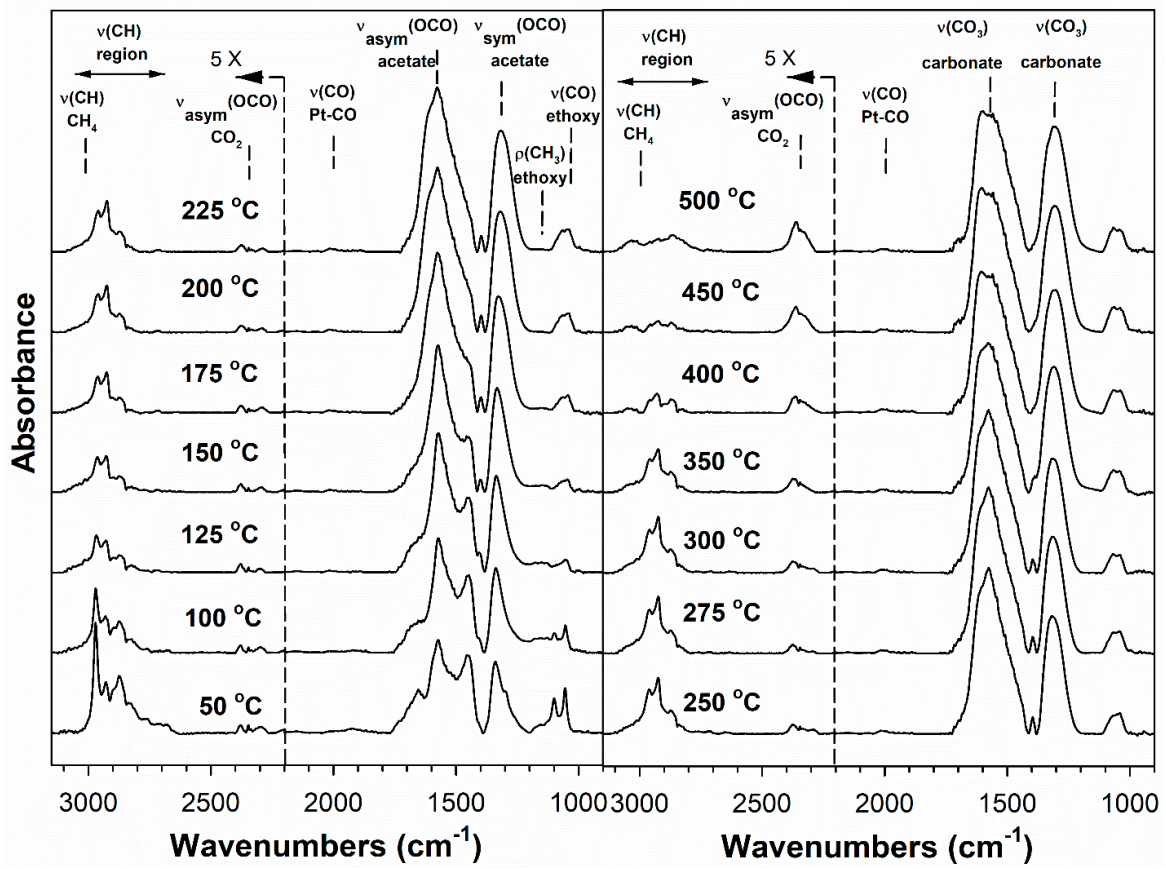

Figure 10. DRIFTS of transient ethanol steam reforming over 10.4% Cs-2% Pt/ZrO_2.

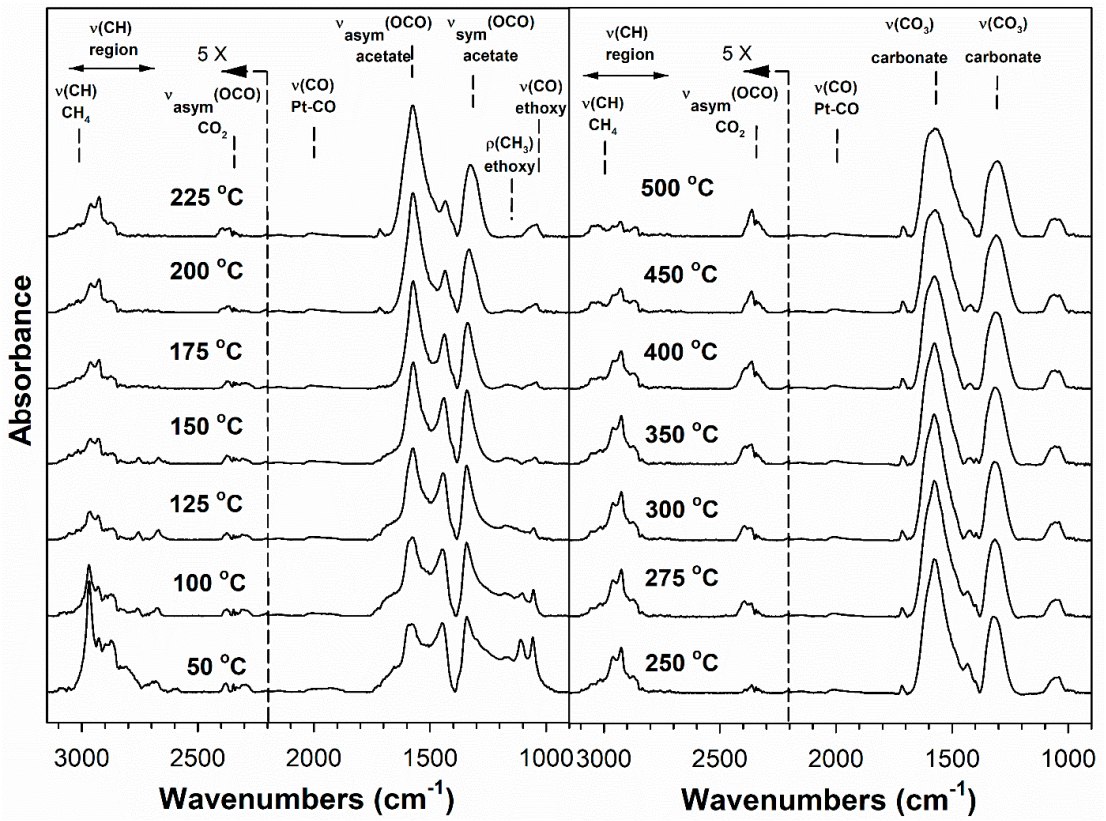

Figure 11. DRIFTS of transient ethanol steam reforming over 14.5% Cs-2% Pt/ZrO_2.

The formation of acetate is an important step in predisposing the catalyst selectivity toward decarboxylation/demethanation at low temperature over the decarbonylation pathway. In comparing Figures 4–11, one can clearly see that the switch in dominant band from 2970 cm^{-1} (ethoxy) to 2930 cm^{-1} (acetate) occurs at lower temperature with increasing addition of Cs up to 5.8% Cs, including the following: unpromoted, 175 °C; 2.9% Cs, 175 °C; 3.9% Cs, 150 °C; 4.8% Cs, 150 °C; and 5.8% Cs, same intensity at 125 °C. Above that loading, the temperature for the transition begins to increase again: 7.2% Cs, 150 °C; 10.4% Cs, same intensity at 150 °C; and 14.5% Cs, same intensity at 150 °C.

Decarbonylation, the non-selective route, is promoted by the metallic function, in this case Pt^0 nanoparticles. With increasing Cs loading, the ν(CO) band of CO adsorbed on Pt decreases, reaching about half the intensity of the unpromoted catalyst by 4.8% Cs and achieving near complete blocking of Pt^0 sites (i.e., very low signal) at 10.4% Cs.

Considering these two aspects—(1) improved decarboxylation of acetate with Cs addition and (2) diminished decarbonylation due to increasing Cs coverage on Pt—it should be expected that methane should form in a more facile manner with Cs addition.

Table 2. IR vibrational wavenumbers in cm^{-1} and mode assignments for the adsorption of ethanol on different catalysts from [25].

Vibrational Mode	Adsorbed Species	Ethanol								
		CeO_2 [a]	Pd/CeO_2 [a]	Pt/CeO_2 [b c]		Pt/TiO_2 [c]	Pt/Al_2O_3 [d]	Ir/Al_2O_3 [e]	$Pt/CeZrO_2$ [f]	$Pt/CeZrO_2$ [g]
$\nu_{as}(CH_3)$	Ethoxy/ acetate	2960	2983	2978	2981	2969	2974	2973	2977	2978
$\nu_{as}(CH_2)$	Ethoxy	–	2934	2933	–	2928	2930	2931	2935	2935
$\nu_s(CH_2)$	Ethoxy	2832	2909	2909	2896	–	2902	2903	2906	2898
$\nu_s(CH_3)$	Ethoxy/ acetate	–	2880	2878	2872	2870	2877	2875	2880	
$\delta(CH_2)$	Ethoxy	1473	1477	1478	-	–	–	-	1473	
$\delta_{as}(CH_3)$	Ethoxy	–	1453	1451	1445	1445	1450	1448	1452	1452
$\delta_s(CH_3)$	Ethoxy	1383	1397	1399	1391	1398	1392	1390		1408
δ(OH)	Molecular ethanol		1266	1264	1264	1267	1276	1277		
$\rho(CH_3)$	Ethoxy	-	-	-	-	1135	1161	1166		
ν(CO) mono	Ethoxy	1107	-	-	1100	-	1106	1118		
ν(CO) mono	Ethoxy		1086	1082	1072	1076	1073	1095	1081	1081
ν(CO) bi	Ethoxy	1057	1039	1038	1042	1040	1052	1052	1045	1045
$\nu_{as}(OCO)$	Acetate	1580				1550	1570	1560	1545	1550
δ_{as} (CH_3)	Acetate	1437								
$\nu_s(OCO)$	Acetate	1426				1460	1472	1478	1425	1425
δ_s (CH_3)	Acetate	1304							1350	1342
$\nu_{as}(OCO)$	Carbonate	1568	1527	1530					1538	
$\nu_s(OCO)$	Carbonate	1428	1442	1423					1431	
$\nu_s(OCO)$	Carbonate	1341	1349	1353						
ν(CO)	Acet-aldehyde		1704	1692			1693		1703	
ν(CO)	Croton-aldehyde		1659		1647	1635				
ν(C=C)	Croton-aldehyde		1637		1613					
ν(CO)	Acetyl									1627
ν(CO)	Ads. CO (bridged)					1970			1938	
ν(CO)	Ads. CO (linear)				2012	2030	2017	2019	2033	2027

[a] Reference [26]; [b] Reference [27]; [c] Reference [28]; [d] Reference [29]; [e] Reference [30]; [f] Reference [31]; [g] Reference [31] under SR reaction mixture.

Table 3. Main bands in cm^{-1} observed for unpromoted and Cs-promoted 2% Pt/m-ZrO_2 catalysts.

Bands	0% Cs	2.9% Cs	3.9% Cs	4.8% Cs	5.8% Cs	7.2% Cs	10.4% Cs	14.5% Cs
				50 °C				
ν(CO) ethoxy	1065, 1052	1100, (1069), 1056	1099, (1069), 1055	1097, 1056	1097, 1055	1097, 1056	1099, 1054	1111, 1057
ν(CH) ethox/acet	2970, 2926	2972, 2929	2999–2969, 2929	2973, 2929	2976, 2932	2971, 2929	2970, 2929	2968, 2927
ρ(CH_3) ethoxy	1150	1156, 1128	1155, 1128	1155, 1129	1157, (1157)	1147, 1127	(1177–1130)	(1169–1125)
ν_a(OCO) acetate	1552	1568	1571, (1512)	1570	1569	1566, (1516)	(1590), 1574, (1562, 1545, 1505)	1593–1577
ν_s(OCO) acetate	(1464), 1429	1471, 1430	1474, (1429), 1410	1464, 1408	1468, (1449), 1406	(1478, 1460), 1406	(1486–1469), 1452	1447
δ_s (CH_3) acetate	1377–1271	1380, 1342	1381, (1357), 1345	1380, 1352, (1342)	(1378), 1350, 1339	(1347), 1334	1339, (1301)	(1378), 1342, (1299)
ν(CO) Pt–CO	2056, (2025–1860)	2054, 1976, (2033–1850)	2053, 1967 (2030–1867)	2009, 1954, (1934–1860)	(2050, 2030, 2005), 1951, (1951–1845)	2002, 1929	2012, 1923	1998, 1927
				175 °C				
ν_a(OCO) acetate	**1553**	**1566**	**1569**	**1574**	**1576**	**1622**, **1570**	(1601), **1572**, (1560–1544)	**1574**
ν_s(OCO) acetate	(1466), **1441**	1471, **1436**	1466, **1433**, 1404	1466, 1432, 1398	1466, 1397	1516–1422, 1398	1400	1439, (1407)
δ_s (CH_3) acetate	1342	1326	1329, 1278	1327, 1283	1327, 1311, 1288	1309	1327, (1296)	1337, (1307)
ν(CH) acetate	2961, **2929**, 2869	3000, 2966, **2931**, 2847	2999, 2976, 2969, **2929**, (2863, 2846)	3001, 2977, 2967, **2927**, 2871, 2846	2992, 2969, **2930**, 2860	2962, **2924**, (2894, 2876, 2856)	2962, (2939), **2925**, 2897, 2874, 2858	2996, 2962, **2925**, 2896, 2871–2862
				500 °C				
ν_a(OCO) carbonate	(1576), 1521	1625, 1580	1623, 1579, (1555–1510)	1630, 1580–1500	1623, 1582–1515	1612, (1567–1420)	1604, (1576–1417)	(1594), 1573, (1545–1426)
ν_s(OCO) carbonate	1469, 1446	1481, 1453	1450	1459	1485–1460	(1567–1420)	(1576–1417)	(1545–1426)
ν_s(OCO) carbonate	1403, 1325	1403, 1351, 1278	1402, 1270	1400, 1273	1289, 1277	(1316), 1291	1334, 1304	(1337), 1306, (1306–1210)

In Figures 4–11, the ν(CH) band occurs at ≈3015 cm^{-1}. For unpromoted 2% Pt/m-ZrO_2 (Figure 4) and for the case of low levels of Cs (e.g., 2.9% and 3.9% Cs, Figures 5 and 6), the ν(CH) band for gas phase CH_4 is pronounced starting at 150 °C. With Cs levels in the 4.8–5.8%, the ν(CH) band for gas phase CH_4 occurs at 125 °C, and at 7.2% Cs, the band is detected at 100 °C. Above that loading (10.4% and 14.5% Cs), the band is observed starting at 125 °C.

Demethanation is accompanied by the formation of adsorbed CO_2 species on the catalyst, including carbonates. While some gas phase CO_2 is detected, the ν(OCO) bands (see Table 3) for surface carbonates are much clearer in DRIFTS spectra. Figure 4 shows that the bands of surface carbonates are highly attenuated even by 400 °C for the unpromoted 2% Pt/m-ZrO_2 catalyst. However, by increasing the loading of Cs, there is a signal for bands of surface carbonates even up to 500 °C, and the intensity of carbonate bands is higher at higher loadings. This indicates that Cs addition increases the basicity of the catalyst, as CO_2 is an acidic molecule that interacts with the catalyst surface.

The results of temperature-programmed reaction of ethanol and water (Figure 12) support the trends from DRIFTS spectroscopy. For the unpromoted 2% Pt/m-ZrO_2 catalysts, there are weak peaks for CH_4 formation at 100 °C and 200 °C and then a strong asymmetric peak starting at 300 °C that peaks at approximately 400 °C. With increasing dopant loadings of Cs, the peaks at low temperature increase and the strong peak shifts to 250 °C in the range of 5.8–7.2% Cs loading. Above that loading, the peaks are attenuated

overall and tend to shift to higher temperature once the exposed Pt is lost due to virtually complete coverage by Cs.

Thus, based on the results of DRIFTS spectroscopy and temperature-programmed reaction, it is expected that the selectivity to decarboxylation/demethanation should be increased with the addition of Cs. By increasing the loading of Cs, there should exist an optimum loading that maximizes the decarboxlation/demethanation selectivity.

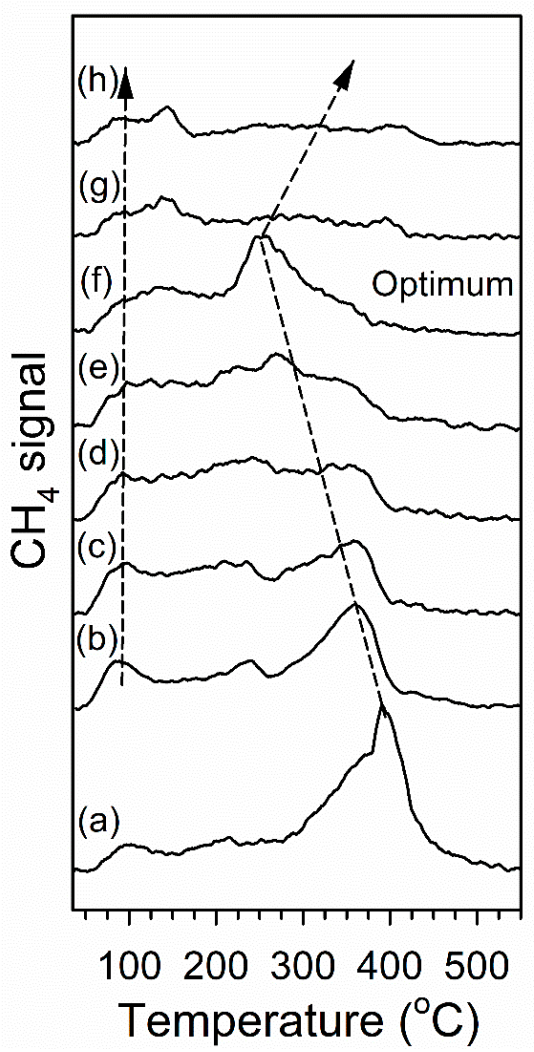

Figure 12. TP-reaction-MS of ethanol steam reforming over (**a**) 2% Pt/ZrO_2, (**b**) 2.9% Cs-2% Pt/ZrO_2, (**c**) 3.9% Cs-2% Pt/ZrO_2, (**d**) 4.8% Cs-2% Pt/ZrO_2, (**e**) 5.8% Cs-2% Pt/ZrO_2, (**f**) 7.2% Cs-2% Pt/ZrO_2, (**g**) 10.4% Cs-2% Pt/ZrO_2, and (**h**) 14.5% Cs-2% Pt/ZrO_2.

Table 4 shows that the addition of Cs, as well as increasing the Cs dopant level, tend to decrease the ethanol conversion rate. This is expected due to the finding that Cs tends to block Pt^0 sites. The addition of 0.7% Cs decreased ethanol conversion by 11%, the addition of 2.9% Cs decreased it by 16%, and adding 5.8% Cs decreased it by 27%. However, the selectivity changes are remarkable. Neglecting other minor pathways, the decarboxlation route accounted for 57.4% versus 42.6% for decarbonylation. With the addition of 0.7% Cs, the percentages shifted to 81.1% versus 18.9% in favor of decarboxylation. For 1.5% Cs, the percentages were 87.6% versus 12.4%. At 2.9% Cs and 5.8% Cs, decarbonylation was negligible, and the catalysts were highly productive for the selective decarboxylation route. The selectivity was compared at similar ethanol conversion between unpromoted and Cs-promoted catalyst (Table 5). The CO selectivity for unpromoted catalyst is always higher than 20% even at lower conversion; in contrast, the CO selectivity is lower than 10%

for low alkali loading (i.e., 0.7 or 1.5%Cs) or zero for high alkali loading (i.e., 2.9 or 5.8% Cs).

Table 4. ESR activity for different Cs loading (300 °C, 1 atm, 19,0560 Ncc/h/g_{cat}, feed: C_2H_5OH 2.98%/H_2O 26.14%/N_2 70.88%).

Catalyst	Conv. C_2H_5OH (%)	C-Selectivity (%)						
		CH_4	CO_2	CO	C_2H_6	C_2H_4	C_3H_6	CH_3CHO
2% Pt/ZrO_2	86.91	45.20 ± 2.26	28.5 ± 1.42	21.16 ± 1.05	0.92 ± 0.04	0.39 ± 0.02	0.34 ± 0.02	3.49 ± 0.34
0.7% Cs-2% Pt/ZrO_2	77.45	48.41 ± 2.42	40.40 ± 2.02	9.44 ± 0.47	0.40 + 0.02	-	-	1.35 ± 0.14
1.5% Cs-2% Pt/ZrO_2	78.42	48.02 ± 2.4	44.66 ± 2.23	6.33 ± 0.32	0.31 ± 0.02	-	-	0.68 ± 0.07
2.9% Cs-2% Pt/ZrO_2	72.95	53.76 ± 2.69	45.62 ± 2.28	-	-	-	-	0.62 + 0.06
5.8% Cs-2% Pt/ZrO_2	63.45	55.74 ± 2.77	43.88 ± 2.17	-	-	-	-	0.68 ± 0.07

Table 5. ESR activity for 2%Pt/ZrO_2 at different C_2H_5OH conversion (300 °C, 1 atm, feed: C_2H_5OH 2.98%/H_2O 26.14%/N_2 70.88%).

Catalyst	Conv. C_2H_5OH (%)	C-Selectivity (%)						
		CH_4	CO_2	CO	C_2H_6	C_2H_4	C_3H_6	CH_3CHO
2%Pt/ZrO_2	86.91	45.20 ± 2.26	28.5 ± 1.42	21.16 ± 1.05	0.92 ± 0.04	0.39 ± 0.02	0.34 ± 0.02	3.49 ± 0.34
	68.90	43.62 ± 2.16	18.21 ± 0.88	28.34 ± 1.45	0.66 ± 0.03	0.52 ± 0.02	0.43 ± 0.02	8.60 ± 0.86
	58.55	47.46 ± 2.37	14.86 ± 0.74	28.37 ± 1.41	0.37 ± 0.02	0.57 ± 0.03	0.36 ± 0.02	7.98 ± 0.80

The underlying reason for the selectivity changes may stem from electronic and/or geometric modifications to the catalyst surface structure. In our recent work on WGS with Cs addition [20], there is clearly an electronic modification of the formate intermediate, as the ν(CH) band is shifted to lower wavenumbers by addition of Cs, as well as with increasing Cs loading (Figure 13). This shift in band position is consistent with a weakening of the C–H bond. Therefore, for the analogous acetate intermediate shown in Scheme 1, one would expect a similar weakening of the C–C bond of acetate, which should favor demethanation/decarboxylation. It is difficult to directly measure this effect, although the evidence for CH_4 being produced at lower temperature in DRIFTS and temperature-programmed reaction experiments provide some support. One additional piece of evidence is that the difference in position of the ν(OCO) asymmetric and symmetric bands changes after adding Cs, and there are further changes with increasing loading of Cs. Such a trend was also observed for the ν(OCO) asymmetric and symmetric bands of formate in our recent WGS work [20]. Examining Table 3, for the unpromoted catalyst, this difference is Δ 112 cm^{-1}; for example, adding Cs, the difference changes as follows: Δ 130 cm^{-1} for 2.9% Cs; Δ 136 cm^{-1} for 3.9% Cs; and Δ 142 cm^{-1} for 4.8% Cs. Thus, there is certainly an electronic modification of the acetate species.

Figure 14 was discussed in our prior work on WGS [20]. The possibility that the alkali may be donating electron density to Pt has been proposed in the past for certain catalysts. If this were the case, then the difference between the L_3 and L_2 XANES spectra should decrease by adding Cs, with further decreases at additional loadings of Cs. As shown in Figure 14, the opposite trend was in fact found. Therefore, it is not possible to conclude that an electronic effect was brought about by electron enrichment of Pt nanoparticles.

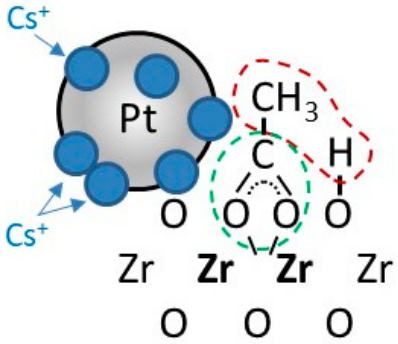

Scheme 1. The effect of an optimal loading of Cs^+ on the decomposition selectivity of acetate intermediate is C–C bond weakening, promoting scission to CO_2 and CH_4.

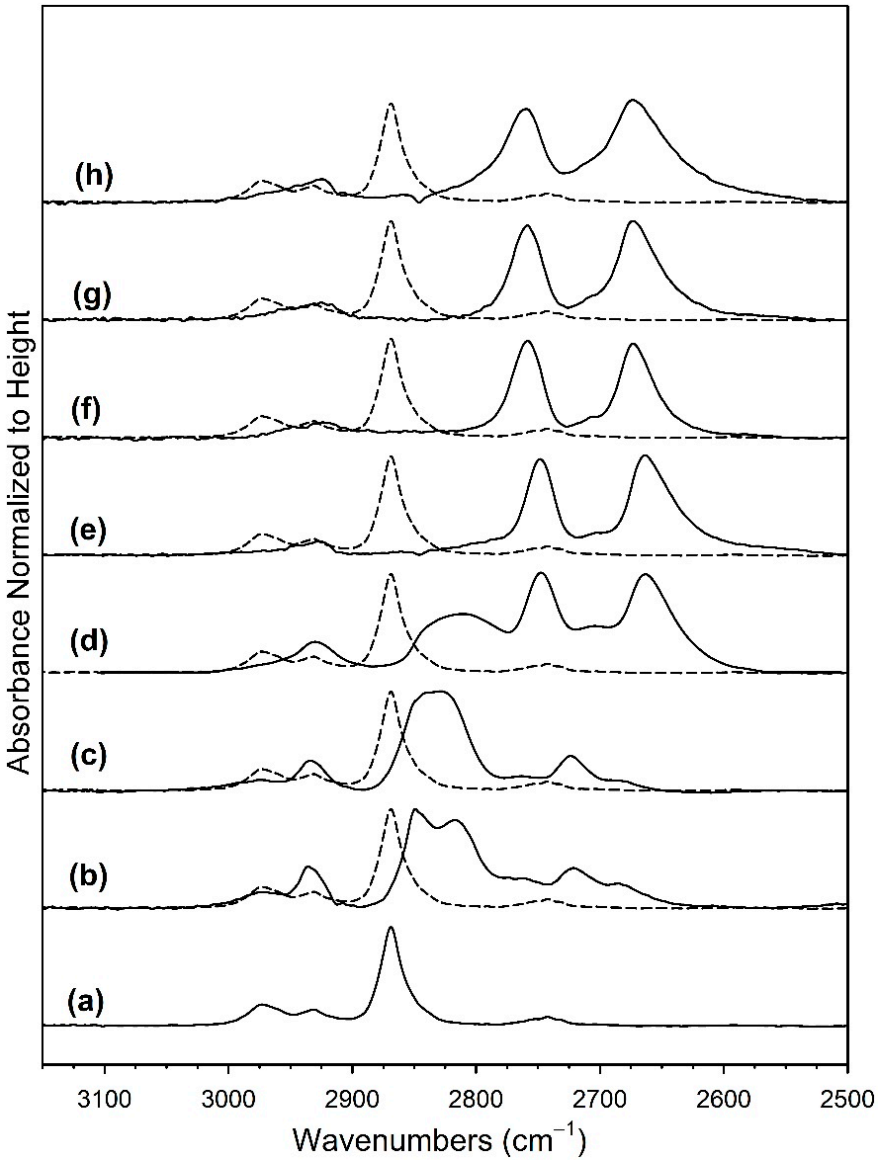

Figure 13. Absorbance of the formate ν(CH) band region normalized to height of band on 2% Pt/ZrO_2, including (**a**) 2% Pt/ZrO_2, (**b**) 2.9% Cs-2% $PtZrO_2$, (**c**) 3.9% Cs-2% Pt/ZrO_2, (**d**) 4.8% Cs-2% Pt/ZrO_2, (**e**) 5.8% Cs-2% Pt/ZrO_2, (**f**) 7.2% Cs-2% Pt/ZrO_2, (**g**) 10.4% Cs-2% Pt/ZrO_2, and (**h**) 14.5% Cs-2% Pt/ZrO_2 (reprinted from [20] with permission from Catalysts, MDPI).

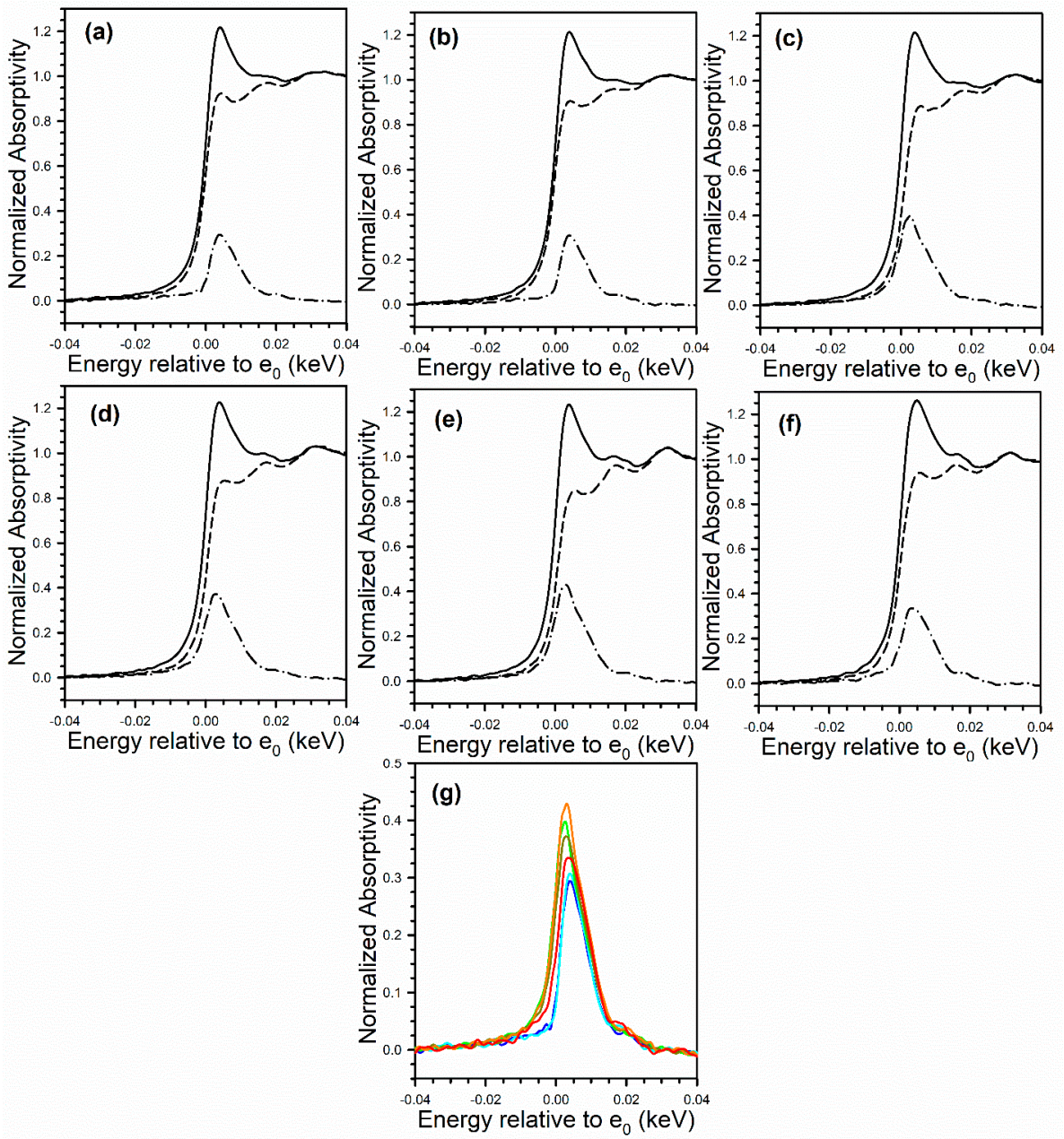

Figure 14. XANES spectra at the Pt (solid line) L_3 edge and (dashed) line L_2 edge, as well as (dash-dotted line) the L_3–L_2 difference spectra of (**a**) 2% Pt/ZrO_2, (**b**) 2.9% Cs-2% Pt/ZrO_2, (**c**) 4.8% Cs-2% Pt/ZrO_2, (**d**) 5.8% Cs-2% Pt/ZrO_2, (**e**) 10.4% Cs-2% Pt/ZrO_2, (**f**) 14.5% Cs-2% Pt/ZrO_2, and (**g**) overlays of L_3–L_2 difference spectra, showing an increase in intensity with Cs loading. No evidence for e^- transfer to Pt from Cs was found, which should result in an opposite trend (reprinted from [20] with permission from Catalysts, MDPI).

Figures 15 and 16 provide an analysis of the energy position of the Pt L_3 and Pt L_2 edge jumps, respectively, for the Pt metal foil (recorded simultaneously with the catalyst) and the catalysts. If there was an electron transfer effect from the Cs promoter to the Pt metal, resulting in an enrichment in the electron density of Pt nanoparticles, then the expected result would be a shift in the edge jump energy to lower energy, due to less core-shell screening. However, comparing the edge energies of the catalysts relative to the Pt metal foil, the edge energies of the catalysts are always slightly higher, with the value ranging from 0.1 to 0.7 eV. Therefore, once again, there is no direct evidence in this work to suggest that an electron enrichment of Pt nanoparticles is responsible for more facile C–C bond

scission of acetate (in this work) or more facile C–H bond scission of formate (prior WGS work [20]).

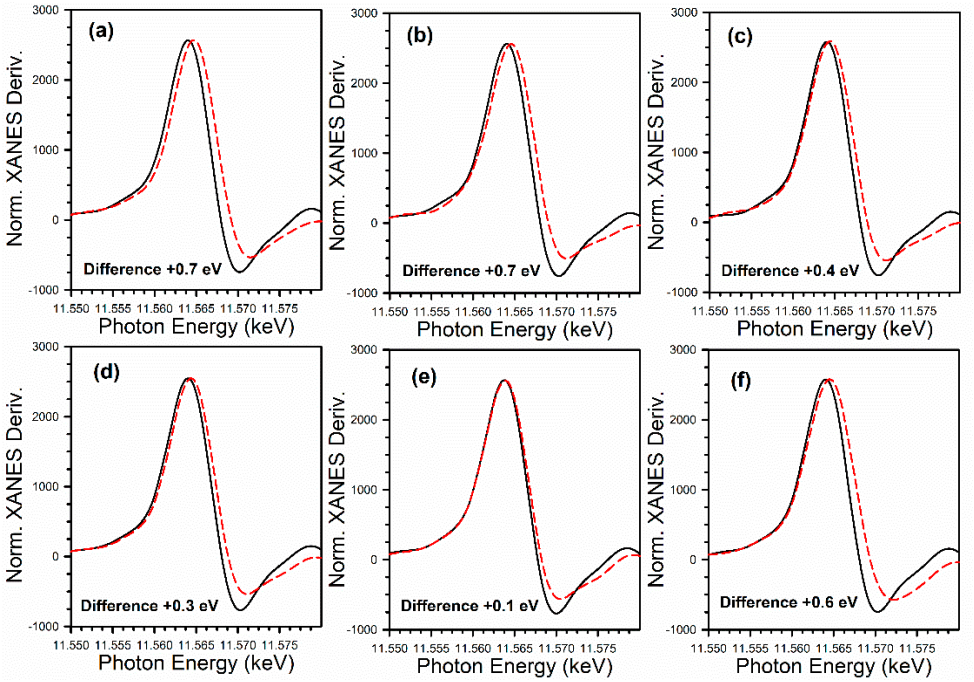

Figure 15. XANES derivative spectra at the Pt L_3 edge that are normalized to the height of the Pt metal foil of (solid black line) Pt metal foil reference and catalysts, including (**a**) 2%Pt/ZrO_2, (**b**) 2.9% Cs-2% Pt/ZrO_2, (**c**) 4.8% Cs-2% Pt/ZrO_2, (**d**) 5.8% Cs-2%Pt/ZrO_2, (**e**) 10.4% Cs-2% Pt/ZrO_2, (**f**) 14.5% Cs-2% Pt/ZrO_2.

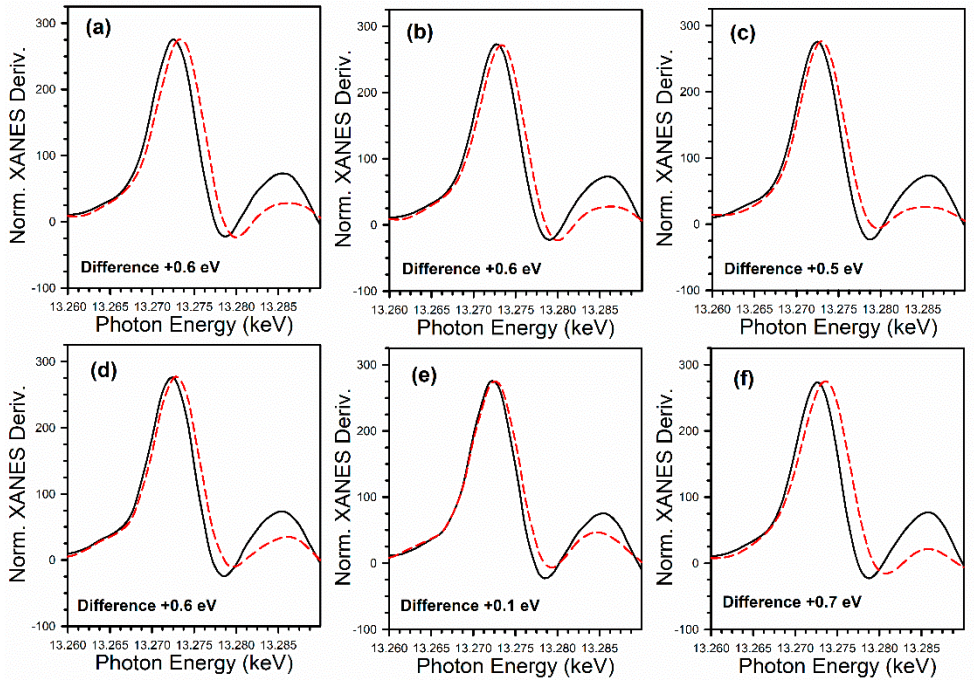

Figure 16. XANES derivative spectra at the Pt L_2 edge that are normalized to the height of the Pt metal foil of (solid black line) Pt metal foil reference and catalysts, including (**a**) 2% Pt/ZrO_2, (**b**) 2.9% Cs-2% Pt/ZrO_2, (**c**) 4.8% Cs-2% Pt/ZrO_2, (**d**) 5.8% Cs-2% Pt/ZrO_2, (**e**) 10.4% Cs-2% Pt/ZrO_2, (**f**) 14.5% Cs-2% Pt/ZrO_2.

Based on the results of characterization and the influence of Cs, the following summary can be made. The selective mechanism of ethanol steam reforming at low temperature involves the dissociation of ethanol to form Type II ethoxy species, which is followed by the oxidative dehydrogenation of ethoxy species to acetate and then forward decomposition of acetate to methane and carbonate, which is the precursor of CO_2. With increasing Cs loading, there is an increase in catalyst basicity. This is observed by more carbonate, the precursor to CO_2 evolution, being retained on the catalyst surface at high temperature (500 °C). This increase in basicity is also likely responsible for the more facile C–C bond breaking occurring in the acetate intermediate, which is consistent with the observation that methane evolved from the catalyst surface at lower temperatures in both DRIFTS and temperature-programmed ESR reaction tests. In prior WGS studies, a decreasing ν(CH) band position of formate with increasing Cs dopant level gave an indication of greater C–H bond weakening in formate. This was accompanied by a greater splitting in wavenumber position between the ν(OCO) asymmetric and symmetric stretching bands. A similar splitting was observed between the ν(OCO) asymmetric and symmetric stretching bands of the acetate intermediate, which was formed from the oxidative dehydration of ethoxy species. This splitting, accompanied by a lower temperature for CH_4 evolution, suggests that Cs addition results in an electronic modification of the acetate intermediate that favors C–C scission, promoting the decarboxylation/demethanation pathway.

Interestingly, near complete selectivity to decarboxylation was achieved at just 2.9% Cs, whereas this occurred at 1.8% Na by weight [19]. However, on an atomic basis, 1.8% Na corresponds to 10.4% Cs. That is, 2.9% Cs is atomically equivalent to 0.5% Na. Thus, Cs is more efficient at promoting decarboxylation than Na. This may be due to a different electronic effect (e.g., Cs is a softer, more diffuse cation than Na), it may be attributed to its higher basicity, resulting in a rearrangement in bond strengths that favors decarboxylation. Another consideration is that there may be a geometric effect that results in more efficient inhibition of Pt-catalyzed decarbonylation. For example, Cs has a larger ionic radius than Na (181 versus 116 pm). Since the decarboxylation pathway ultimately favors higher selectivity to hydrogen over the decarbonylation route, these catalysts could foreseeably be used to convert ethanol to H_2 and CH_4 at low temperature for feeding into a conventional methane steam reforming for the production of hydrogen with higher selectivity.

3. Materials and Methods

3.1. Catalyst Preparation

Unpromoted and cesium-doped 2% Pt/m-ZrO_2 catalysts were prepared with diverse loadings (0.7%, 1.5%, 2.2%, 2.9%, 3.9%, 4.8%, 5.8%, 7.2%, 10.4%, or 14.5% by weight) of Cs. Monoclinic phase zirconia (230 mesh and 120 mesh sieves to provide particles in the range of approximately 63–125 μm) (No. 43815, Alfa Aesar, Haverhill, MA, USA) was impregnated with 2% Pt using aqueous $Pt(NH_3)_4(NO_3)_2$ (No. 88960, Alfa Aesar, Haverhill, MA, USA) by incipient wetness impregnation (IWI). After calcination for 4 h in a muffle furnace at 350 °C, the catalyst was divided into several portions and was promoted by aqueous $CsNO_3$ (No. 12884, Alfa Aesar, Haverhill, MA, USA) by IWI. Impregnation was followed by drying and re-calcining at 350 °C for four hours using a muffle furnace.

3.2. Catalyst Characterization

3.2.1. H_2-Temperature-Programmed Reduction (TPR) and TPR-Mass Spectrometry

Temperature-programmed reduction (TPR) was conducted on the catalysts utilizing an Altamira AMI-300R (Pittsburgh, PA, USA) instrument coupled to a mass spectrometer from Hiden Analytical (Warrington, UK). The procedure entailed flowing 10% H_2/He (Airgas, USA) while ramping temperature from 50 to 1000 °C at a heating rate of 10 °C/min.

3.2.2. In Situ Diffuse Reflectance Infrared Fourier Transform Spectroscopy

Temperature desorption/reaction experiments were conducted using a Nicolet iS-10 Fourier Transform infrared spectrometer (Thermo Fisher, Waltham, MA, USA) in diffuse

reflectance mode, coupled with an in situ Harrick Scientific Praying Mantis cell (Pleasantville, New York, NY, USA). The catalyst was reduced at 300 °C using 100 cm^3/min H_2 and 100 cm^3/min He for 1 h and then cooled to 50 °C in H_2. Then, ethanol was bubbled using helium (75 cm^3/min) for ≈15 min. Then, helium was used to bubble water (31 °C water bath), resulting in an H_2O concentration of 4.4% with a flow rate of 75 cm^3/min, which was used to react with adsorbed ethanol species, converting it to acetate, which was followed by decarbonylation and/or decarboxylation of acetate depending on the catalyst composition as the temperature was stepped in 50 °C increments from 50 to 500 °C.

3.2.3. Temperature-Programmed Reaction with Mass Spectrometry

A temperature-programmed reaction was also carried out with the Altamira AMI-300R unit coupled with the Hiden mass spectrometer. The catalyst was reduced at 300 °C using 10 cm^3/min H_2 and 20 cm^3/min argon for 1 h. Then, the catalyst was cooled to 50 °C in argon, and ethanol at 100 cm^3/min was pumped into the system for 10 min, which was followed by an argon purge (20 min in 30 cm^3/min argon). Next, H_2O was bubbled in helium (30 cm^3/min) for 10 min, which was followed by purging in argon. Then, argon was flowed at 30 cm^3/min while the temperature was increased to 700 °C to conduct steam reforming of the adsorbed ethanol. The signal of methane was followed to examine the effect of Cs doping on C–C scission.

3.2.4. X-ray Diffraction

X-ray diffraction (XRD) was carried out using a Rigaku Ultima IV diffractometer (RIGAKU, Tokyo, Japan) equipped with a dual position graphite diffracted beam monochromator for Cu, using a Cu Kα radiation at 43 kV and 30 mA.

3.2.5. TEM-STEM

TEM analysis was performed with FEI Talos F200X microscope (Thermo Fisher Scientific, Waltham, MA, USA) equipped with bright field (BF), dark field (DF) 2, DF4, and high-angle annular dark-field (HAADF) detectors. The elemental distributions were determined via FEI super energy-dispersive X-ray spectroscopy (EDX) (Thermo Fisher Scientific, Waltham, MA, USA). The imaging was collected with a field emission gun using an accelerating voltage of 200 kV and a high speed Ceta 16M camera. Velox software was used for data processing. Prior to the analysis, the samples were dispersed in ethanol, sonicated for 30 min, and then, a droplet of the suspension was added to a carbon-coated copper grid (300 mesh) and dried in air overnight.

3.2.6. EXAFS/XANES

The Materials Research Collaborative Access Team (MR-CAT) beamline at the Advanced Photon Source in Argonne National Laboratory was used to conduct in situ H_2-EXAFS experiments. Incident energies were selected via a Si (1 1 1) monochromator in conjunction with a Rh-coated mirror to remove non-fundamental harmonics of the beam energy. Jacoby describes an experimental setup similar to that used in this work [32]. In situ TPR was conducted on six samples simultaneously using a multi-sample holder (3 mm i.d. channels) made of stainless steel. Self-supporting wafers were loaded into each channel using roughly 6 mg of catalyst, which is an amount optimized for the Pt L_3 edge on a ZrO_2 support. The multi-sample holder was placed inside a clamshell furnace mounted on the positioning table. The quartz tube is outfitted with Kapton view ports and ports for gas and a thermocouple. Samples were aligned with the beam with 20 μm precision for repeat scans. After positioning, the quartz tube was purged with 100 mL/min He for at least 5 min. Afterward, 100 mL/min pure hydrogen was flowed, and the temperature was increased to 350 °C at a rate of 1.0 °C/min. Spectra at the Pt L_3 edge were taken in transmission made with Pt^0 foil serving as a reference for energy calibration. EXAFS spectra were analyzed using WinXAS (Version 2.0, Thorsten Ressler, Berlin, Germany) [33]. Fitting of EXAFS Spectra was carried out with Atoms [34], FEFF [35], and FEFFIT [35] using

spectra from the end of the TPR (after the temperature had been ramped to 350 °C and subsequently cooled in flowing H_2). Fittings were performed from 3 to 10 $Å^{-1}$ in k-space. The inner Pt–Pt coordination shell was isolated by applying a Hanning window of the Fourier transformed spectra and subsequently performing the inverse Fourier transform. Fittings were performed from 1.85 Å to 3.25 Å in R space.

3.3. Catalytic Testing

The activity of the catalysts was tested in a homemade fixed bed reactor. Briefly, 80 mg of catalyst (63–106 μm) was diluted with 300 mg of SiO_2 beads and activated using 100 cm^3/min H_2 at 350 °C for 1 h. Next, the temperature was cooled to 300 °C, and the gas feed was switched to a mixture containing 26.1% H_2O, 2.9% C_2H_5OH (balance N_2) at P = 1 atm, gas hourly space velocity (GHSV) = 190,560 $Ncm^3/min/g_{cat}$. Then, the products were passed through a cold trap (held at 5 °C) to collect condensable compounds. The condensable products were analyzed by SRI (SRI Instruments, Torrance, CA, USA) 8610 GC equipped with HayeSep Q-column, whereas the gas products were analyzed by Inficon micro-GC Fusion equipped by molecular sieve, alumina, plot-u, and OV-1. The ethanol conversion (3) and the carbon selectivity (4) were calculated using the following formula:

$$\chi_{C_2H_5OH} = 1 - \frac{F^{out}_{C_2H_5OH}}{F^{in}_{C_2H_5OH}} \quad (3)$$

$$S_i = \frac{n_i \cdot F_i^{out,\ prod}}{\sum_i n_i \cdot F_i^{out,prod}} \quad (4)$$

where $F^{in}_{C_2H_5OH}$ is the inlet molar flow of ethanol, $F^{out}_{C_2H_5OH}$ is the outlet molar flow, n_i is the carbon number, and $F_i^{out,\ prod}$ is the outlet molar flow of the produced carbon species (i = CO, CO_2, CH_4, C_2H_6, C_2H_4, C_3H_6, C_2H_4O).

4. Conclusions

DRIFTS and the temperature-programmed reaction of ethanol steam reforming as well as fixed bed catalyst testing revealed that the addition of Cs promotes the decarboxylation/demethanation pathway over decarbonylation by increasing the basicity of the catalyst and weakening the C–C bond of the acetate intermediate, facilitating its scission. There exists an optimum loading of Cs that is sufficient to promote C–C scission without excessively blocking Pt sites on tiny (0.78–1.4 nm) Pt nanoparticles that are necessary for promoting H-transfer reactions. The addition of just 2.9% Cs promoted decarboxylation and virtually nullified the unselective decarbonylation route with a decrease in ethanol conversion of just 16%. In comparison with our previous work with Na, this amount is—on an equivalent atomic basis—just 28% of the amount of Na that is required to achieve the same effect. The C–C scission pathway involving acetate decarboxylation ultimately favors a higher selectivity to hydrogen over the decarbonylation route if the methane produced is subsequently reformed. As such, these catalysts could be used in the foreseeable future to convert ethanol to H_2 and CH_4 at low temperature, which is followed by subsequent feeding into a conventional methane steam reformer to improve hydrogen productivity.

Author Contributions: Conceptualization, formal analysis, investigation, supervision, visualization, validation, writing, G.J., Z.R., and M.M. Formal analysis, investigation, validation, writing, L.J. and C.D.W. Formal analysis, investigation, validation, D.Q. Supervision, investigation, resources, D.C.C. Data curation, investigation, resources, supervision, A.J.K. All authors have read and agreed to the published version of the manuscript.

Funding: Caleb D. Watson would like to acknowledge support from the Undergraduate NSF Research Program, supported by the National Science Foundation through grant award #1832388.

Acknowledgments: Argonne's research was supported in part by the U.S. Department of Energy (DOE), Office of Fossil Energy, National Energy Technology Laboratory (NETL). Advanced photon source was supported by the U.S. Department of Energy, Office of Science, Office of Basic Energy Sciences, under contract number DE-AC02-06CH11357. MRCAT operations are supported by the Department of Energy and the MRCAT member institutions. CAER research was supported by the Commonwealth of Kentucky. Caleb D. Watson would like to acknowledge funding from a UTSA College of Engineering Scholarship. Gary Jacobs would like to thank UTSA and the State of Texas for financial support through startup funds. We also thank Shelley D. Hopps at the University of Kentucky Center for Applied Energy Research for assistance with the X-ray diffraction measurements.

Conflicts of Interest: The authors declare no conflict of interest.

References

1. AMIS Market Monitor No. 48—May 2017. Available online: http://www.amis-outlook.org/fileadmin/user_upload/amis/docs/Market_monitor/AMIS_Market_Monitor_Issue_47.pdf (accessed on 20 July 2021).
2. Ziolkowska, J.R. Biofuels technologies: An overview of feedstocks, processes, and technologies. In *Biofuels for a More Sustainable Future*; Ren, J., Scipioni, A., Manzardo, A., Liang, H., Eds.; Elsevier: Amsterdam, The Netherlands, 2020; pp. 1–19.
3. Jayasinghe, S. *Cellulosic ethanol: Beyond the kernel. Renewable Energy Report*; Agricultural Marketing Resource Center (AgMRC) at Iowa State University: Ames, IA, USA, 2016; Available online: https://www.agmrc.org/renewable-energy/renewable-energy-climate-change-report/renewable-energy-climate-change-report/july-2016-report/cellulosic-ethanol-beyond-the-kernel (accessed on 20 July 2021).
4. Hanson, S. Renewable Natural Gas Increasingly Used to Meet Part of EPA's Renewable Fuel Requirements. Today in Energy, Energy Information Agency; 2017. Available online: https://www.eia.gov/todayinenergy/detail.php?id=33212 (accessed on 20 July 2021).
5. Dole, M.; Wilson, F.R.; Fife, W.P. Hyperbaric hydrogen therapy: A possible treatment for cancer. *Science* **1975**, *190*, 152–154. [CrossRef] [PubMed]
6. Ohno, K.; Ito, M.; Ichihara, M. Molecular hydrogen as an emerging therapeutic medical gas for neurodegenerative and other diseases. *Oxidative Med. Cell. Longev.* **2012**, *2012*, 353152. [CrossRef]
7. Wang, C.; Li, J.; Liu, Q.; Yang, R.; Zhang, J.H.; Cao, Y.-P.; Sun, X.-J. Hydrogen-rich saline reduces oxidative stress and inflammation by inhibit of JNK and NF-kappaB activation in a rat model of amyloid-beta-induced Alzheimer's disease. *Neurosci. Lett.* **2011**, *491*, 127–132. [CrossRef] [PubMed]
8. Ohsawa, I.; Ishikawa, M.; Takahashi, K.; Watanabe, M.; Nishimaki, K.; Yamagata, K.; Katsura, K.-I.; Katayama, Y.; Asoh, S.; Ohta, S. Hydrogen acts as a therapeutic antioxidant by selectively reducing cytotoxic oxygen radicals. *Nat. Med.* **2007**, *13*, 688–694. [CrossRef] [PubMed]
9. Ohta, S. Molecular hydrogen is a novel antioxidant to efficiently reduce oxidative stress with potential for the improvement of mitochondrial diseases. *Biochim. Biophys. Acta* **2012**, *1820*, 586–594. [CrossRef] [PubMed]
10. Rostrup-Nielsen, J.R. Conversion of hydrocarbons and alcohols for fuel cells. *Phys. Chem. Chem. Phys.* **2001**, *3*, 283–288. [CrossRef]
11. Jacobs, G.; Davis, B.H. In situ DRIFTS investigation of the steam reforming of methanol over Pt/ceria. *Appl. Catal. A Gen.* **2005**, *285*, 43–49. [CrossRef]
12. De Lima, S.M.; Silva, A.M.; Graham, U.M.; Jacobs, G.; Davis, B.H.; Mattos, L.V.; Noronha, F.B. Ethanol decomposition and steam reforming of ethanol over $CeZrO_2$ and $Pt/CeZrO_2$ catalyst: Reaction mechanism and deactivation. *Appl. Catal. A Gen.* **2009**, *352*, 95–113. [CrossRef]
13. Ciambelli, P.; Palma, V.; Ruggiero, A. Low temperature catalytic steam reforming of ethanol. 1. The effect of the support on the activity and stability of Pt catalysts. *Appl. Catal. B Environ.* **2010**, *96*, 18–27. [CrossRef]
14. He, Z.; Yang, M.; Wang, X.; Zhao, Z.; Duan, A. Effect of the transition metal oxide supports on hydrogen production from bio-ethanol reforming. *Catal. Today* **2012**, *194*, 2–8. [CrossRef]
15. Brooks, C.; Cypes, S.; Grasselli, R.K.; Hagemeyer, A.; Hogan, Z.; Lesik, A.; Streukens, G.; Volpe, A.F.; Turner, H.W.; Weinberg, W.H.; et al. High throughput discovery of CO oxidation/VOC combustion and water–gas shift catalysts for industrial multi-component streams. *Top. Catal.* **2006**, *38*, 195–209. [CrossRef]
16. Pigos, J.M.; Brooks, C.J.; Jacobs, G.; Davis, B.H. Low temperature water-gas shift: Characterization of Pt-based ZrO_2 catalyst promoted with Na discovered by combinatorial methods. *Appl. Catal. A Gen.* **2007**, *319*, 47–57. [CrossRef]
17. Martinelli, M.; Alhraki, N.; Castro, J.D.; Matamoros, M.E.; Jacobs, G. Water-gas shift: Effect of Na loading on Pt/m-zirconia catalysts for low-temperature shift for the production and purification of hydrogen. In *New Dimensions in Production and Utilization of Hydrogen*; Elsevier: Amsterdam, The Netherlands, 2020; pp. 143–160.
18. Jacobs, G.; Keogh, R.A.; Davis, B.H. Steam reforming of ethanol over Pt/ceria with co-fed hydrogen. *J. Catal.* **2007**, *245*, 326–337. [CrossRef]
19. Martinelli, M.; Castro, J.D.; Alhraki, N.; Matamoros, M.E.; Kropf, A.J.; Cronauer, D.C.; Jacobs, G. Effect of sodium loading on Pt/ZrO_2 during ethanol steam reforming. *Appl. Catal. A Gen.* **2021**, *610*, 117947. [CrossRef]

20. Rajabi, Z.; Martinelli, M.; Watson, C.D.; Cronauer, D.C.; Kropf, A.J.; Jacobs, G. Influence of Cs loading on Pt/m-ZrO_2 water-gas shift catalysts. *Catalysts* **2021**, *11*, 570. [CrossRef]
21. Jentys, A. Estimation of mean size and shape of small metal particles by EXAFS. *Phys. Chem. Chem. Phys.* **1999**, *1*, 4059–4063. [CrossRef]
22. Marinković, N.S.; Sasaki, K.; Adzic, R.R. Nanoparticle size evaluation of catalysts by EXAFS: Advantages and limitations. *Zaštita Mater.* **2016**, *57*, 101–109. [CrossRef]
23. Binet, C.; Daturi, M.; Lavalley, J.-C. IR study of polycrystalline ceria properties in oxidised and reduced states. *Catal. Today* **1999**, *50*, 207–225. [CrossRef]
24. Martinelli, M.; Jacobs, G.; Shafer, W.D.; Davis, B.H. Effect of alkali on CH bond scission over Pt/YSZ catalyst during water-gas-shift, steam-assisted formic acid decomposition and methanol steam reforming. *Catal. Today* **2017**, *291*, 29–35. [CrossRef]
25. Mattos, L.V.; Jacobs, G.; Davis, B.H.; Noronha, F.B. Production of hydrogen from ethanol: Review of reaction mechanism and catalyst deactivation. *Chem. Rev.* **2012**, *112*, 4094–4123. [CrossRef]
26. Yee, A.; Morrison, S.J.; Idriss, H. A study of the reactions of ethanol on CeO_2 and Pd/CeO_2 by steady state reactions, temperature programmed desorption, and in situ FT-IR. *J. Catal.* **1999**, *186*, 279–295. [CrossRef]
27. Yee, A.; Morrison, S.J.; Idriss, H. A study of ethanol reactions over Pt/CeO_2 by temperature-programmed desorption and in situ FT-IR spectroscopy: Evidence of benzene formation. *J. Catal.* **2000**, *191*, 30–45. [CrossRef]
28. Raskó, J.; Dömök, M.; Baán, K.; Erdőhelyi, A. FTIR and mass spectrometric study of the interaction of ethanol and ethanol-water with oxide-supported platinum catalysts. *Appl. Catal. A Gen.* **2006**, *299*, 202–211. [CrossRef]
29. Dömök, M.; Toth, M.; Raskó, J.; Erdőhelyi, A. Adsorption and reactions of ethanol and ethanol-water mixture on alumina-supported Pt catalysts. *Appl. Catal. B Environ.* **2007**, *69*, 262–272. [CrossRef]
30. Erdőhelyi, A.; Raskó, J.; Kecskes, T.; Toth, M.; Dömök, M.; Baan, K. Hydrogen formation in ethanol reforming on supported noble metal catalysts. *Catal. Today* **2006**, *116*, 367–376. [CrossRef]
31. De Lima, S.M.; da Cruz, I.O.; Jacobs, G.; Davis, B.H.; Mattos, L.V.; Noronha, F.B. Steam reforming, partial oxidation and oxidative steam reforming of ethanol over Pt/$CeZrO_2$ catalyst. *J. Catal.* **2008**, *257*, 356–368. [CrossRef]
32. Jacoby, M. X-ray absorption spectroscopy. *Chem. Eng. News* **2001**, *79*, 33. [CrossRef]
33. Ressler, T. WinXAS: A program for x-ray absorption spectroscopy data analysis under MS-Windows. *J. Synchrotron Radiat.* **1998**, *5*, 118. [CrossRef]
34. Ravel, B. ATOMS: Crystallography for the X-ray absorption spectroscopist. *J. Synchrotron Radiat.* **2001**, *8*, 314–316. [CrossRef]
35. Newville, M.; Ravel, B.; Haskel, D.; Rehr, J.J.; Stern, E.A.; Yacoby, Y. Analysis of multiple-scattering XAFS data using theoretical standards. *Phys. B Condens. Matter* **1995**, *208*, 154–156. [CrossRef]